

Role of sublimation kinetics of ammonia borane in chemical vapor deposition of uniform, large-area hexagonal boron nitride

Balaji Sompalle^{1,2}, Chun-Da Liao¹, Bin Wei¹, M Fatima Cerqueira^{1,2}, Nicoleta Nicoara^{1,3}, Zhongchang Wang¹, Sascha Sadewasser^{1,3}, and Pedro Alpuim^{1,2,3,a}

¹International Iberian Nanotechnology Laboratory, Braga, Portugal

²Department of Physics, University of Minho, Braga, Portugal

³QuantaLab, International Iberian Nanotechnology Laboratory, Braga, Portugal

^aElectronic mail: pedro.alpuim.us@inl.int

ABSTRACT

Hexagonal boron nitride, h-BN, is a critical 2D insulator used as a substrate, gate dielectric, or encapsulation layer for graphene and other 2D materials and their van der Waals heterostructures. It is also promising as an active layer in single-photon emitters and other photonic devices. With chemical formula $\text{H}_3\text{N}-\text{BH}_3$, ammonia borane is the most attractive precursor for up-scalable growth of large-area h-BN, using chemical vapor deposition given its stoichiometric B:N ratio, high stability under ambient conditions, non-toxicity, and high solubility in common solvents. Here, the synthesis of large-area (100 mm \times 150 mm) crystalline hexagonal boron nitride layers by thermal activation and decomposition of the precursor ammonia borane is presented. We describe two different reaction pathways for h-BN synthesis, providing evidence for dis-similarities in the sublimation kinetics of ammonia borane and how these differences critically influence the growth of h-BN. This understanding helps us accelerate h-BN production, re-use precursors, and reduce machine runtime, paving the way for upscalability. Moreover, our work provides a consistent unified view explaining the diverse deposition conditions reported in the literature for h-BN grown by CVD using ammonia borane as a precursor.

I. INTRODUCTION

Two-dimensional materials (2D) have shown unique properties that make them strong candidates for flexible, transparent electronics in applications such as gas sensors, biosensors, and photodetectors.^{1,2} The interest has increased since chemical vapor deposition (CVD) of these materials was shown to be an alternative to the artisanal non-scalable exfoliation technique used in the early stage of 2D materials research.^{3,4} Since many of these materials are the single layer constitutive unit of bulk 3D layered crystals, exfoliation is possible. Exfoliated flakes are attractive for research because they present high structural and electronic quality at a relatively low cost since the exfoliation technique itself involves virtually no, or residual, equipment costs.⁵ However, deterministic control of the process and scalability are also virtually impossible. CVD is the preferred choice for 2D materials growth, translating the scientific achievements in 2D materials science into a practical technology because of its potential to yield large and controllable atomic layers with minimal contamination. In particular, CVD has been used to deposit h-BN with some degree of success, using different precursors, depending on the laboratory and the application sought. However, so far, only a very limited number of groups can deposit h-BN with electronic quality over large areas.⁶⁻⁹ A clear discussion about the unfavorable sublimation kinetics of ammonia borane (AB) hinders attempts to attain the desired results. H-BN is traditionally considered the "perfect", atomically flat substrate and encapsulation layer to fabricate devices using other 2D materials, namely graphene.¹⁰ Also, it gained tremendous attention from the photonics community since the demonstration of single-photon emission from structural defects at room temperature.¹¹

Hexagonal boron nitride is an in-plane hexagonal arrangement of B and N atoms in a honeycomb structure. It is structurally similar to graphene, where one triangular sublattice is formed by B-atoms and the other by N-atoms. Both bond length and interlayer distance being equal in h-BN, and in graphene, h-BN is sometimes referred to as white graphene.¹² Unlike graphene, however, the B-N bond is slightly ionic due to the difference in electronegativity between B (2.04) and N (3.04).¹³ The chemical asymmetry between the B and N sub-lattices also determines the band structure of h-BN with an indirect bandgap at 5.955 eV at RT,¹⁴ responsible for its electrically insulating properties.

Ammonia borane (AB), with the chemical formula H_3BNH_3 , also called borazane, has attracted much interest in the past as a promising solid-state hydrogen storage material due to its high hydrogen storage capacity (19.6 wt %).¹⁵ AB is non-flammable and non-explosive under ambient conditions and has 1:1 B:N stoichiometry, which favors the formation of h-BN. AB is chosen instead of borazine because it is stable in the ambient atmosphere, whereas borazine hydrolyzes to orthoboric acid, ammonia, and hydrogen in the presence of moisture. Steady synthesis of h-BN from AB is impeded by unfavorable sublimation kinetics, for example, shifting of melting temperature, long induction period, excessive hydrogen release steps, and formation of oligomeric compounds.¹⁵ Thermodynamic properties of AB have been reported as early as the 1950s. However, the mechanism and important intermediates leading to h-BN accompanied by hydrogen release were not fully understood until 2007 when Autrey et al.¹⁶ detailed the physical and chemical transformation of AB during induction, nucleation, and growth stages.

Liu *et al.* grew a self-limiting 10 nm thick h-BN layer using ammonia borane as the precursor, using 1000°C growth temperature, 30-60 minutes growth time, and varying precursor partial pressure.¹⁸ Kim *et al.* obtained polycrystalline films with domain sizes <10 nm using AB as precursor at 1000°C, 350 mTorr, and 10-120 minutes growth time; AB was sublimated at 60-90°C.⁹ Lee *et al.* and Guo *et al.* also demonstrated polycrystalline films with domain sizes <10nm using AB as precursor at 1000°C growth temperature.²³ None of the above groups discussed precursor sublimation, by-products, and layer control. Han *et al.* installed a filter sheet at the precursor inlet line to avoid unwanted by-products of AB decomposition.²⁰

There is no agreement in the literature regarding the temperature to use for the AB sublimation. While a few reports describe sublimation at temperatures as low as 40 to 60 °C, others report sublimation between 110 and 150 °C^{6,9,17,18-26}, as shown in Figure 1(a). No detailed mechanistic and kinetic studies of AB sublimation for h-BN synthesis are available. Also, a correlation between the h-BN growth and the precursors' sublimation is not reported. Conclusive evidence regarding the occurrence of melting point depression of AB has not been found. Finally, there is a limited understanding of the AB sublimation mechanism leading to crystalline h-BN.

This is the author's peer reviewed, accepted manuscript. However, the online version of record will be different from this version once it has been copyedited and typeset.
PLEASE CITE THIS ARTICLE AS DOI: 10.1116/1.50000987

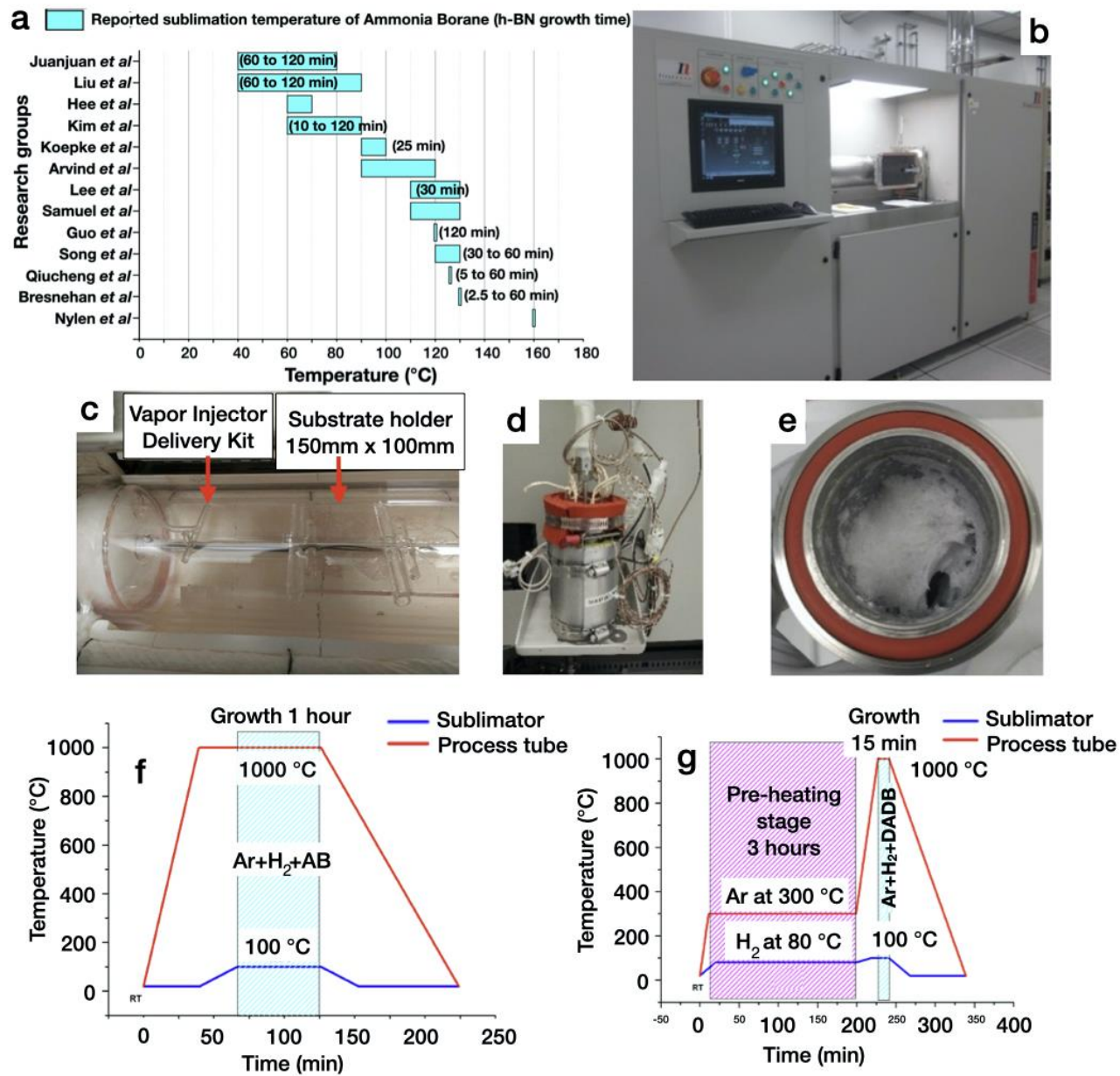


Figure 1: (a) Sublimation temperature of AB reported in the literature. Higher sublimation temperature corresponds to reduced growth time. (b) Chemical vapor deposition system at the facility. (c) Detail of quartz tube with vapor injector and partial view of the 150 mm × 100 mm substrate holder. (d) Solid source sublimator. (e) Solid source sublimator reservoir with powder AB converted to a mixture of DADB and PAB after preheating. (f) Schematic illustration of the h-BN growth process pathway A, where the deposition is carried out without prior heat treatment. (g) Schematic illustration of h-BN growth process pathway B, where AB is preheated at 80 °C for 3 hours to suppress the melting point.

Here, we present the controlled synthesis of hexagonal boron nitride films by regulating the sublimation of solid ammonia borane. The main focus is on growing continuous films of thickness from 4 to 10 nm, which is more realistic and suitable for large-scale device development than single-layer films.^{17,27-28} Our findings advance the understanding of h-BN synthesis and helps to establish an industrial process for continuous h-BN production.

II. MATERIALS AND METHODS

Our CVD system (First Nano ET3000, see Figure 1(b)) comprises a hollow cylindrical quartz process tube of 5" outer diameter that can accommodate substrates measuring up to 10 cm × 15 cm. It has a load lock chamber with a cantilevered quartz arm for automatic loading/unloading of the samples. The temperature is cascade controlled up to 1200°C within the three-zone resistively-heated furnace. Temperature feedback is provided by three type-K thermocouples axially placed inside the furnace (one per zone, protected by a glass sheath). Unlike simpler models of CVD reactors where the solid precursor is placed inside the main process tube, the CVD ET3000 has a dedicated preheating reservoir as shown in Figure 1(c) with independent control of the temperature, in the reservoir, in the flange, and the ¼" stainless steel tubing. The CVD is equipped with an injector delivery kit (Figure 1(d)), capable of showering the sample substrate with a vapor precursor.

Thermal preheating was performed in the closed-loop sublimation reservoir of CVD ET3000. The reservoir has a heating range of 60-180 °C and has three discrete heating elements: body, flange, and heating line. All the heaters can be independently controlled for temperature set point and heating rate. The reservoir is connected to an H₂ gas line with

the regulated flow from 0 to 50 sccm controlled by a GF40 Brooks mass flow controller. The temperatures, gas flows, and other deposition parameters are software controlled by the CVDWinPrC₂ software suite.

Ammonia borane was obtained from Sigma-Aldrich (97% purity). The growth substrate is 25 μm thick, high purity (99.99%) copper foil obtained from Goodfellow. The growth of h-BN was carried out following two different pathways. In pathway A (Figure 1 (g)), 300 mg of AB is put in the cell (Figure 1(e)). The process tube is heated to 1000 $^{\circ}\text{C}$ and the sublimator cell to 100 $^{\circ}\text{C}$. The carrier gas H₂ was introduced into the sublimator, which brings the vapor precursor to the process tube. A 4:1 mixture of Ar:H₂ with flow rates of 200:50 sccm was simultaneously delivered to the process tube. Typical growth lasts from 60 to 120 minutes to grow h-BN films with thicknesses ranging from 4 nm to 10 nm.

In pathway B (Figure 1(h)), around 300 mg of AB was introduced in the cell (similar to pathway A). The cell was then heated to 80 $^{\circ}\text{C}$ at 3 $^{\circ}\text{C}/\text{min}$. The set temperature was maintained for 3 hours, followed by cooling down to room temperature at ~ 3 $^{\circ}\text{C}/\text{min}$. This preheating step transforms AB to di-ammoniate di-borane (Figure 1(f)), suppressing the melting point, further discussed below. After the three-hour induction period, the process tube was heated to 1000 $^{\circ}\text{C}$, and the sublimator cell was heated to 100 $^{\circ}\text{C}$. H₂ carrier gas is introduced into the sublimator, bringing the precursor to the process tube. A 4:1 mixture of Ar:H₂ with flow rates of 200:50 sccm is delivered to the process tube (similar to pathway A). Typical growth lasts for 15 minutes to grow h-BN films of 4 nm to 10 nm.

The preheating process reduces the machine run time by a factor of four, as compared to pathway A. The thickness of the film was regulated by adjusting the partial pressure of the

AB vapor. The sublimation behavior is sensitive to such parameters as sublimation pressure, container temperature, sublimation time, requiring consistent control over the sublimation process. Such control can be effectively achieved using a separate sublimation reservoir, allowing further flexibility to control these parameters. After h-BN growth on Cu foil, h-BN is transferred with a PMMA (630 nm) thick supporting layer, wherein copper is etched using a 0.7 molar iron chloride solution. After the PMMA/h-BN is released, it is subjected to a cleaning process by alternate dipping in 2% HCl for 30 minutes and DI water for 5 minutes. This process is repeated five times to remove any unwanted metal contaminants effectively. After the cleaning process, the stack is transferred to the target substrate by scooping it out of the DI water. Post transfer, the stack is annealed at 180°C for 12 hours for better adhesion. The last steps include removing PMMA using acetone and cleaning the sample with water and IPA and drying it using nitrogen.

Raman spectra were acquired at room temperature in backscatter geometry using a WiTec Alpha 300R confocal system equipped with a 532 nm frequency-doubled Nd-YAG laser. Data is collected with 600 g/mm or 1800 g/mm gratings at 50× magnifying objective lens for a laser power level ~10 mW. The acquisition time was between 10 and 20 s. Raman of h-BN on Cu did not yield any visible signal due to background reflection by the Cu substrate. Hence the Raman measurements were performed on h-BN films transferred onto Si/SiO₂ substrates.

X-ray photoelectron spectroscopy data were acquired by ESCALAB 250 Xi system with an analysis chamber maintained in UHV conditions all the time. The chemical composition of the samples can be analyzed with a depth resolution of 1-10 nm. The measurements were performed for h-BN directly grown on a Cu surface without any treatment. A transferred

sample was discarded because of a strong Si 2s plasmon loss feature that overlaps the B1s region. A survey scan was performed to identify the prominent peaks, after which high-resolution scans over narrow regions were performed. A large number (50) of scans was used when acquiring the B1s spectrum. The data was then adjusted with the Cu peak as a reference. Scanning electron microscope analysis was performed on FEI NovaNanoSEM 650, equipped with a cold field emission electron source. The measurements were acquired with accelerating voltages of 3-10 kV. A transmission electron microscope (TEM) was used to study the atomic structure of h-BN. The high-resolution TEM images were obtained using an FEI TITAN aberration-corrected TEM (Themis) equipped with the high-angle annular dark-field (HAADF) and the bright field (BF) imaging techniques, operating at 80 kV.

Energy-dispersive X-ray spectroscopy (EDS) was used to characterize the elemental information of the as-prepared samples. Optical images were acquired using a Nikon Eclipse L200 N microscope with a motorized stage and a 10X objective with a 60 mm focal distance. Images were processed with NIS Elements-D software. Amplitude-modulated Kelvin probe force microscopy (KPFM) was performed in a Bruker Dimension Icon atomic force microscope (AFM) operated in an ambient environment, using the dual-pass method with a lift height of 5 nm. Pt/Ir coated cantilevers (POINTPROBE-PLUS® Silicon-SPM-Sensor from Nanosensors™) with a nominal tip radius of 25 nm, a spring constant of 42 N/m, and 295 kHz resonance frequency were used. The tips were calibrated using an Au-coated Si sample to ensure the comparability of the results. The contact potential difference (CPD) is defined as $CPD = e(\Phi_{tip} - \Phi_{sample})$, where Φ is the work function.

III. RESULTS AND DISCUSSION

A. Properties of the films grown by pathways A and B

Raman spectroscopy is a quick, effective, and rapid method to identify the presence of h-BN and elucidate the number of layers in a given sample. Figure 2(a) shows the Raman spectra of h-BN samples obtained from both A and B pathways, overlapped for easy comparison. According to the peak at 1370 cm^{-1} , h-BN obtained from both pathways has similar thicknesses and more than three layers. The peak is due to B-N bond stretching vibrations. It is the same mode as the G band in graphene, corresponding to an E_{2g} vibration in h-BN.²⁹ The Raman shifts of the 1 L, 2 L, > 3 L (L stands for layer), and bulk films, grown by CVD in this work are 1372 , 1370.5 , 1369.9 , and 1368 cm^{-1} , respectively (Figure 2(b)). The monolayer gives a very weak E_{2g} peak. As the number of layers increases, the peak intensity increases proportionally (Figure 2(b)). As previously reported in the literature, peak shifts of $\pm 1\text{ cm}^{-1}$ can be observed in otherwise similar samples because of substrate-induced strain.³⁰ For comparison, the Raman signature of a commercial monolayer sample (Graphene Supermarket) shows a peak at 1371.4 cm^{-1} . Figure 2(c) is an optical image of the h-BN transferred sample, obtained by pathway B, showing the $100 \times 100\text{ }\mu\text{m}^2$ area enclosed by a red square where the Raman surface scans are performed with a resolution of 50×50 pixels. Figure 2(d) shows the corresponding Raman map, with red color tone proportional to the integrated intensity of the Raman peak around 1370 cm^{-1} . The proportionality constant is found by comparison with the base spectrum statistically representative of all Raman spectra in the analyzed area shown in Figure 2(e). The image demonstrates the total surface coverage of h-BN. These data show that homogeneous growth of h-BN is achieved over large areas.

This is the author's peer reviewed, accepted manuscript. However, the online version of record will be different from this version once it has been copyedited and typeset.
PLEASE CITE THIS ARTICLE AS DOI: 10.1116/1.6.0000987

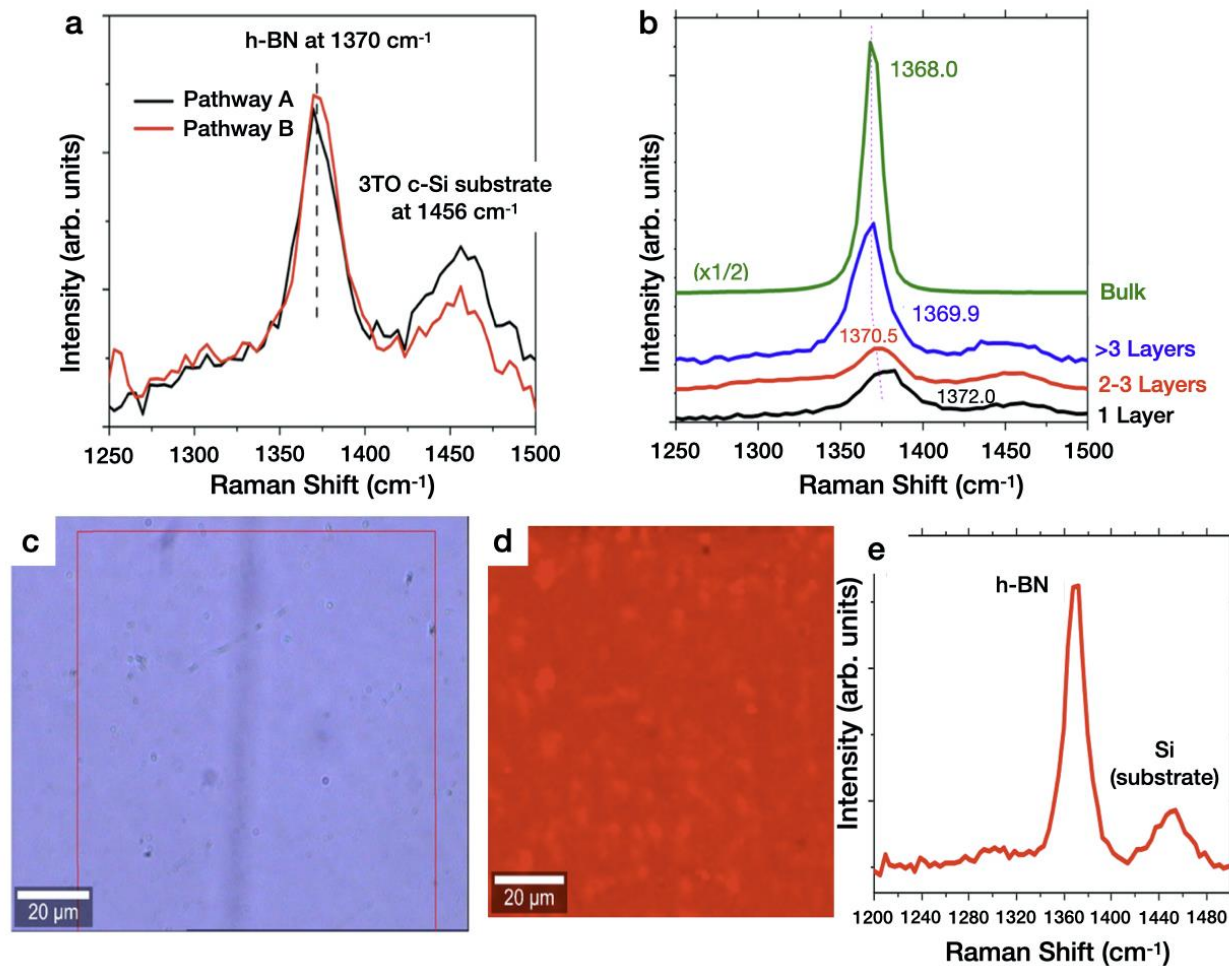


Figure 2 (a) Raman mode comparison in h-BN samples obtained by pathway A and pathway B. According to the peak position, the h-BN obtained from both pathways is of the same thickness (~ 4 nm). (b) h-BN Raman mode peak position as a function of the number of h-BN layers. (c) An optical image of a sample with an area of 100×100 mm² shows full surface coverage. (d) Raman map of the red-boxed area as in (c) acquired with a resolution of 50×50 pixels. Color code is given by the red base spectrum shown in (e).

Morphology and surface potential characterization of CVD-grown h-BN films is performed using Kelvin probe force microscopy (KPFM). Representative topography

images of h-BN grown by pathway B on Cu foil are shown in Figure 3 (a,b). For a 30 min CVD process, the Cu substrate is fully covered.

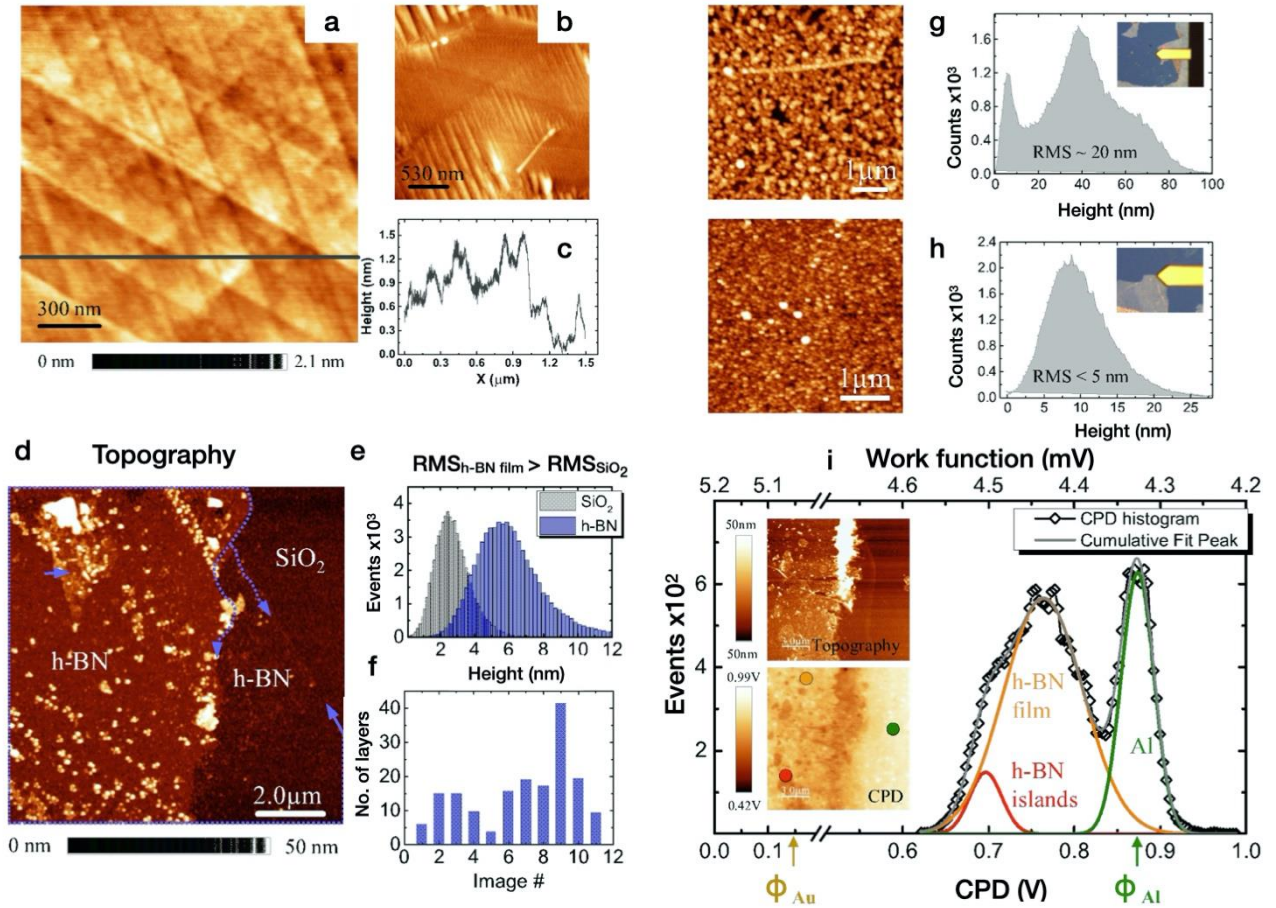


Figure 3 AFM and KPFM results on CVD-grown h-BN on Cu foil and transferred onto SiO₂ or Al/SiO₂ substrates. (a, b) Tapping mode topography of h-BN grown on Cu foil by pathway B. (a) 1.5 μm × 1.5 μm. (b) 3 μm × 3 μm image showing hexagonal and triangular-like structures of the h-BN film formed on the Cu foil. (c) Line profile along the grey line in (a). (d) Topography of h-BN (pathway B) after transfer to SiO₂. (e) Roughness analysis was extracted from h-BN covered areas (blue contour) and h-BN-free SiO₂ areas (grey contour). (f) h-BN thickness distribution extracted from (d). (g, h) Topography of h-BN grown by pathway A and pathway B, transferred onto SiO₂, and corresponding roughness analyses. (i) KPFM of h-BN (grown by pathway B) after transfer onto an Al/SiO₂ substrate. Inset: Topography (top) and CPD map (bottom). Image size: 15 μm × 15 μm. Histogram of the CPD map (open symbols). The top axis represents absolute work function values.

The h-BN film presents a clean surface with a small number of impurities or residues.

The few-layers thick h-BN film grows conformally on the polycrystalline Cu substrate's

stepped surface, forming hexagonal and diamond-shape structures resulting from zigzag termination h-BN sheets, as shown in Figure 3(a) and (b) and similar to what was observed in the literature.^{31,32} The film surface roughness estimated from RMS analysis is < 0.3 nm. Step heights of ~ 3 -4 Å are mainly found, as determined from the line profile in Figure 3(c), in agreement with the reported 3.3 Å interlayer distance in h-BN bulk.³³ Due to overlapping layers in the film, also steps with larger height values of ~ 6.7 Å and ~ 10 Å, multiples of a monolayer (ML) thickness can be found. KPFM characterization of the h-BN layers grown on Cu foil reveals a uniform contact potential difference (CPD) (see Figure S1 for topography and KPFM characterization of a multilayer h-BN film in supplementary material at *hyperlink*).

AFM measurements were also performed on h-BN (grown on Cu foil) transferred either to a SiO₂ or an Al/SiO₂ substrate. The topography image in Figure 3(d) shows the h-BN (grown by pathway B) film partially covering the SiO₂ substrate. The transferred h-BN films do not present the hexagonal-like structure previously observed for the as-grown h-BN on Cu foil; instead, the film appears inhomogeneous and granular, consistent with previous reports.¹⁷ The surface roughness increases when compared to the as-grown h-BN on Cu foil. Representative data are shown in Figure 3(e). From the surface maps analysis, RMS roughness values of $\sim 1.6 \pm 0.1$ nm and 1.1 ± 0.1 nm were determined for the h-BN film and SiO₂ substrate, respectively. The statistical analysis of the height of the film (to the SiO₂ substrate) indicates that the transferred h-BN shows thickness variations between 1.5 and 14 nm (± 0.2 nm). Considering the h-BN interlayer distance of ~ 3.3 Å, this corresponds to 4-40 MLs thick h-BN film. Figure 3(f) shows the h-BN thickness distribution extracted from the AFM images. The reported thickness can be slightly

overestimated since the distance between the substrate and the first h-BN layer cannot be determined from these experiments. Figures 3(g) and (h) compare the results of h-BN films obtained by pathways A and B, respectively. For pathway B, Figure 3(h), the Cu substrate is fully covered, and the h-BN film presents a clean surface with a reduced amount of impurities or residues compared to pathway A. The transferred film of pathway B has estimated surface roughness $RMS < 5$ nm, which is four times less than films obtained by pathway A. We attribute this difference to the controlled vapor delivery of ammonia borane, as explained below. Insets in Figure 3 (g, h) show an optical image of the sample's scanned area, where the h-BN films can be identified due to a contrast difference with the SiO_2 substrate.

KPFM measurements were performed on h-BN films transferred to an Al/ SiO_2 substrate, where Al provides the required metallic contact. The inset in Figure 3(i) shows the topography (top) and the simultaneously acquired CPD map (bottom) of h-BN (grown by pathway B), partially covering the Al/ SiO_2 substrate. The h-BN appears as a continuous film that conformally covers the substrate. This constant h-BN layer thickness is 8.3 ± 0.1 nm, measured to the substrate surface. However, other small islands form on the film leading to a maximum thickness of 14.7 ± 0.1 nm (see Figure S2 for topography and CPD map of h-BN islands in supplementary material at *hyperlink*). Increasing the deposition time to 150 minutes does not affect thickness following the catalytic limit of h-BN growth on copper.^{34,35} Some remnants/residue resulting from the transfer process can remain on the sample surface, as indicated by the bright area in the top-middle part of the topography image in Figure 3(i). The CPD map shows a uniform potential on the Al surface, significant contrast difference at the residue location, and some potential variation on the h-BN film.

The histogram of the contact potential distribution is represented in Figure 3(i); here, the residue area was not taken into account. An excellent fit of the curve is obtained by including three Gaussian contributions for the Al substrate (green line), the continuous h-BN layer (orange line), and the h-BN islands (red line). These results indicate that h-BN layers have a work function of $\Phi_{\text{h-BN}} \sim 4.5 \pm 0.1$ eV, in comparison to $\Phi_{\text{Al}} \sim 4.35 \pm 0.05$ eV, obtained on the Al/SiO₂ substrate.

A thickness-dependent CPD behavior of h-BN films is also observed (Figure S2). An increase of the h-BN thickness by ~ 7 -8 nm (i.e., 20-24 h-BN layers) induced a decrease in the CPD value by ~ 150 mV. From the statistical analysis of the KPFM results, it is concluded that the transfer of the h-BN film increases the work function of the surface, and with a larger thickness of the h-BN film, a further slight increase occurs.

B. Nucleation and growth of h-BN

Figure 4(a,b) shows an optical image of ~ 4 to 8 nm thick h-BN deposited by pathway B and transferred onto a SiO₂ substrate by a polymer-assisted transfer process. It is seen that the edge of the h-BN film retains residues from previous steps, possibly consisting of iron, copper, and polymer. Figure 4 (a) shows a clear contrast between h-BN and bare SiO₂ substrate. Figure 4(b) shows the h-BN layers folded during the transfer process. Figure 4(c) shows an SEM image of h-BN on native Cu substrate, grown at the flow rate of Ar/(H₂+AB) in the ratio of 40:1. It can be seen that h-BN growth starts on the defects or inhomogeneities of the copper surface, namely dislocations, grain boundaries, and triple points that serve as nucleation sites to initiate the growth (squared darker regions in the image are differential charging artifacts from prior scans (low to high magnification)). After this initial stage, the growth proceeds along the few wide terraces edges visible on

This is the author's peer reviewed, accepted manuscript. However, the online version of record will be different from this version once it has been copyedited and typeset.
PLEASE CITE THIS ARTICLE AS DOI: 10.1116/1.6.0000987

the otherwise flat copper surface. The edges of the broad terraces make up a defect site and offer an ideal region for h-BN nucleation to start. Subsequently, incorporating B and N atoms takes place to form a cluster oriented parallel to the edges before expanding over the edges of the remaining copper surface. Figure 4(c) shows that almost all defect sites have anchored a single h-BN crystal (identified by red arrows).

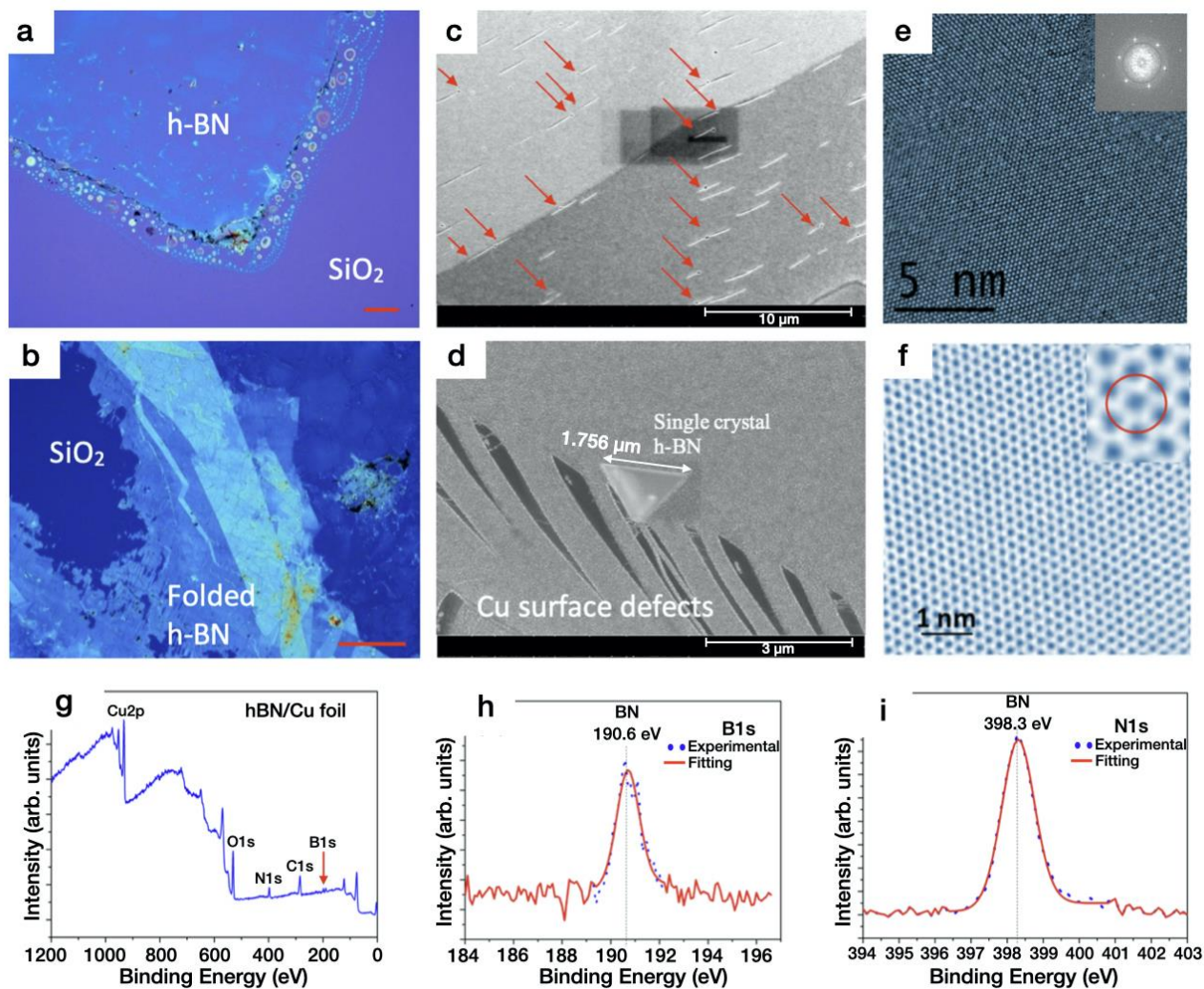


Figure 4 (a) Optical image of h-BN film grown by pathway B and transferred onto Si/SiO₂. Transfer artifacts are visible at the edge of the film. (scale bar 100 μm) (b) Optical image of h-BN film transferred onto Si/SiO₂ showing folded h-BN sheets. (c) SEM image of copper foil with h-BN crystals grown at copper defect sites (marked by red arrow), h-BN covered area of the Cu surface appears darker than the bare one. (d) SEM image of single-crystal h-BN grown at the copper defect site. (e) TEM image of h-BN at 5 nm scale. (f)

Their brightness in transmission microscope image clearly distinguishes individual boron and nitrogen atoms. Every single hexagonal ring of the boron-nitrogen structure, for instance, the one marked by the red circle in the figure, consists of three brighter nitrogen atoms and three darker boron atoms. (g) XPS survey scan of h-BN on Cu foil. (h) High-resolution XPS B 1s spectra of h-BN on Cu. (i) High-resolution XPS N 1s spectra of h-BN on Cu.

This site selectivity is explained by the thermodynamic energy barrier for nucleation at different sites, becoming finite at AB partial pressures higher than a critical value. For example, we do not observe site selectivity when $Ar/(H_2+AB)$ is in the ratio of 4:1; in this case, h-BN starts to grow everywhere on the Cu foil, not necessarily on the defect sites. Figure 4(d) shows a single h-BN crystal anchored at a Cu defect site. Increasing the duration of growth does not help in increasing crystal size.

Further study is needed on how to promote site selectivity and increase single-crystal sizes of h-BN, for example, by pre-oxidation of the Cu substrate. The present results provide additional evidence that h-BN growth has many similarities with that of graphene, except that to form triangular and hexagonal crystals, B and N atoms must be supplied in equal amounts. The B/N ratio estimated by XPS (Figure 4 (g,h,i)) measurements with characteristic peaks of B 1s at 190.6 eV and N 1s at 398.3 eV is 1.14. Figure 4(e) shows TEM images of suspended h-BN transferred onto a TEM grid. The apparent feature observed in the picture is the small-scale periodicity of the honeycomb lattice. Individual B and N atoms can be distinguished separately in the TEM image. Every single hexagonal ring of the boron-nitrogen structure (see, for example, the one marked with the red circle in Figure 4(f)) consists of three brighter nitrogen atoms and three darker boron atoms.

C. Pathways A and B explained by ammonia borane chemistry

The above results show that h-BN obtained by both pathways A and B have the same Raman signature corresponding to a similar thickness and that films obtained by pathway

This is the author's peer reviewed, accepted manuscript. However, the online version of record will be different from this version once it has been copyedited and typeset.
PLEASE CITE THIS ARTICLE AS DOI: 10.1116/6.0000987

B have lower roughness by a factor of four, compared to those from pathway A. h-BN by pathway B is obtained in only 15 minutes deposition time whereas pathway A implies a 60 minutes long deposition time. These differences between pathways A and B stem from the complexity of sublimation kinetics of ammonia borane. Ammonia borane (borazane, H_3NBH_3 , Molecular formula is shown in Figure 5) is formed when a lone pair of electrons in NH_3 forms a dative bond with an empty p_z orbital of boron in BH_3 ¹⁶. AB exists in the form of a colorless or white solid powder at room temperature with a melting point in the range of 110-114 °C.^{36,37} Some reports affirm that ultra-pure AB melts at 125 °C.^{38,39} AB is solid with a dative covalent B-N bond. AB contains both hydridic B-H bonds and protic N-H bonds and a strong B-N bond. In N-H bonds, hydrogen holds a partial positive charge, $\text{H}^{\delta+}$, whereas the hydrogen atom in B-H bonds has a partial negative charge, $\text{H}^{\delta-}$. Interaction of a protic N-bonded H with a hydridic B-bonded H of an adjacent molecule gives rise to dihydrogen bonds.¹⁵ The additional energy of dihydrogen bonds contributes to AB's stability in the solid-state under standard conditions. So under the influence of temperature, molecular hydrogen loss is favored over dissociation to ammonia and borane, finally leading to hexagonal boron nitride.²²

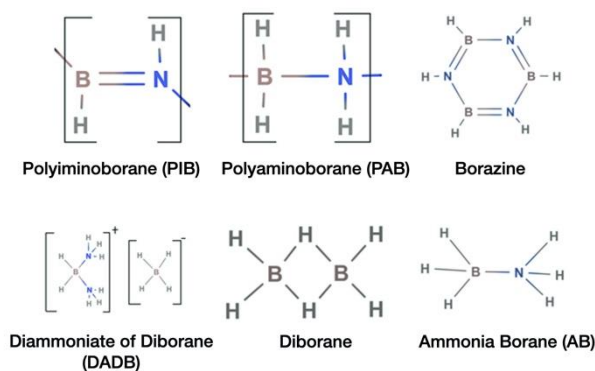
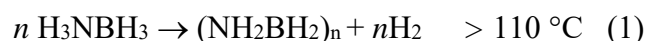


Figure 5 Chemical structural formulae of Boron compounds that are referred to in the text.

Two distinct pathways are leading to hexagonal boron nitride. Pathway A: pyrolytic decomposition of ammonia-borane described by Samuel *et al.*²²: when AB is heated above 110 °C, hydrogen release commences. The first step occurring mostly between 110 to 120 °C, promotes the formation of polyaminoborane (PAB, (NH₂BH₂)_n) and H₂. When heated, these molecules tend to eliminate hydrogen intermolecularly with the formation of a dimer (eq.(1)):



On further heating above 130 °C, PAB undergoes hydrogen loss through both intermolecular processes of cross-linking polymer chains and an intramolecular process of B-N double bond formation, giving polyiminoborane (PIB, (NHBH)_n) and a minute quantity of gas-phase species of borazine (N₃B₃H₆) (eq.(2)):



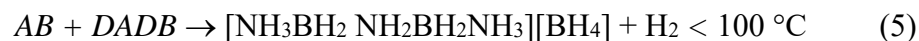
The third process starting at around 1000 °C promotes further cross-linking of PIB, resulting in the semi-crystalline phase hexagonal boron nitride.



When using higher sublimating temperatures (above 100 °C), several groups observed 3D nanoparticles formed on h-BN films on Cu foils. It is reported that the density of these particles increased with sublimation temperatures above 100 °C.^{9,40}

Pathway B: Melting point depression of ammonia-borane due to the formation of intermediate diammoniate of diborane, as detailed in Ref¹⁶. When AB is preheated at 80 °C for 2-4 hours, it is converted into a mixture of diammoniate of diborane (DADB, [(NH₃)₂BH₂]⁺[BH₄]⁻) and PAB. As a result of the conversion from AB to DADB and polymers, the resultant mixture shifts the melting temperature of AB to a lower value. The

accepted scheme of conversion of AB to DADB was described by Autrey *et al.*¹⁶ via three successive steps: induction, nucleation, and growth. During the induction period, dihydrogen bonds are disrupted, followed by the nucleation that transforms AB to reactive DADB (eq.(4)):



The N-H and B-H bonds of DADB are more reactive than the N-H and B-H bonds of AB. But as the reaction progresses, a highly polar environment develops, which stabilizes DADB and leads to a shift in equilibrium concentration towards DADB relative to AB. In the reaction described by Eq. (5), DADB and other dimer species (cyclic or open-chain) can arise simultaneously, causing, in any case, the melting point depression of AB. Further, h-BN is formed by a bimolecular reaction between AB and DADB to release gas-phase B/N species and stored hydrogen.

We performed reactions (4) and (5) at 80 °C and monitored the evolution of the reaction using Raman spectroscopy at fixed time intervals. Figure 6 shows the Raman signatures of the leading chemical species involved in Eqs. (4) and (5), with molecular formulas given in Figure 5: it is seen that the distinctive Raman peaks of AB disappear as AB is polymerized into DADB, which confirms the processes described in Eqs. (4) and (5). Based on this evidence, the dissimilarities of sublimating kinetics during the CVD growth of h-BN by pathways A and B are explained.

This is the author's peer reviewed, accepted manuscript. However, the online version of record will be different from this version once it has been copyedited and typeset.
PLEASE CITE THIS ARTICLE AS DOI: 10.1116/1.6.0000987

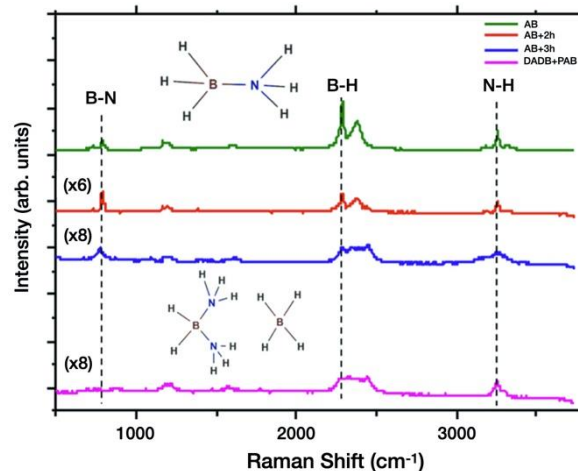


Figure 6 Raman spectra taken at different time intervals showing that crystalline AB isomerizes to DADB during thermal pre-conditioning treatment.

IV. CONCLUSION

In summary, we have demonstrated the growth of high-quality, large-area (100 mm \times 150 mm) hexagonal boron nitride films from thermally pre-conditioned ammonia borane. Prolonged thermal treatment of AB at 80 °C creates adequate impurities for melting point depression to occur. This melting point depression accelerated h-BN synthesis without raising the sublimation temperature. Preheating of AB in a range of temperatures before the deposition step accelerates h-BN synthesis. The formation of oligomers and polymers along with AB and diammoniate of diborane deplete the melting temperature of AB. These findings provide a methodology to accelerate h-BN production by altering the temperature kinetics of solid AB. Characterization results support past observations in the literature and give more insight into the fundamental process leading to h-BN.

ACKNOWLEDGMENTS

This work was supported by National Funds through the Portuguese Foundation for Science and Technology (FCT) in the framework of the Strategic Funding UIDB/04650/2020 and projects PTDC/FIS-NAN/3668/2014 (LA2D) and PTDC/FIS-MAC/28114/2017 (POCI-01-0145-FEDER-028114) (GRAPHSENS).

DATA AVAILABILITY

The data that support the findings of this study are available from the corresponding author upon reasonable request.

REFERENCES

- ¹ S.Z. Butler, S.M. Hollen, L. Cao, Y. Cui, J.A. Gupta, H.R. Gutiérrez, T.F. Heinz, S.S. Hong, J. Huang, A.F. Ismach, E. Johnston-Halperin, M. Kuno, V. V Plashnitsa, R.D. Robinson, R.S. Ruoff, S. Salahuddin, J. Shan, L. Shi, M.G. Spencer, M. Terrones, W. Windl, and J.E. Goldberger, *ACS Nano* **7**, 2898 (2013).
- ² K.S. Novoselov, A. Mishchenko, A. Carvalho, and A.H.C. Neto, *Science* **353**, 6298 (2016).
- ³ K.S. Novoselov, V.I. Fal'ko, L. Colombo, P.R. Gellert, M.G. Schwab, and K. Kim, *Nature* **490**, 192 (2012).
- ⁴ R. Mas-Balleste, C. Gomez-Navarro, J. Gomez-Herrero, and F. Zamora, *Nanoscale* **3**, 20 (2011).
- ⁵ K.S. Novoselov, D. Jiang, F. Schedin, T.J. Booth, V. V Khotkevich, S. V Morozov, and A.K. Geim, *P. Natl. Acad. Sci. Usa* **102**, 10451 (2005).

This is the author's peer reviewed, accepted manuscript. However, the online version of record will be different from this version once it has been copyedited and typeset.
PLEASE CITE THIS ARTICLE AS DOI: 10.1116/1.50000987

- ⁶ J.C. Koepke, J.D. Wood, Y. Chen, S.W. Schmucker, X. Liu, N.N. Chang, L. Nienhaus, J.W. Do, E.A. Carrion, J. Hewaparakrama, and A. Rangarajan, *Chem. Mater.* **28**, 4169 (2016).
- ⁷ R.Y. Tay, M.H. Griep, G. Mallick, S.H. Tsang, R.S. Singh, T. Tumlin, E.H. Teo, and S.P. Karna, *Nano Lett.* **14**, 839 (2014).
- ⁸ A. Ismach, H. Chou, D.A. Ferrer, Y. Wu, S. McDonnell, H.C. Floresca, A. Covacevich, C. Pope, R. Piner, M.J. Kim, and R.M. Wallace, *ACS Nano* **6**, 6378 (2012).
- ⁹ K.K. Kim, A. Hsu, X. Jia, S.M. Kim, Y. Shi, M. Hofmann, D. Nezich, J.F. Rodriguez-Nieva, M. Dresselhaus, T. Palacios, and J. Kong, *Nano Lett.* **12**, 161 (2012).
- ¹⁰ C.R. Dean, A.F. Young, I. Meric, C. Lee, L. Wang, S. Sorgenfrei, K. Watanabe, T. Taniguchi, P. Kim, K.L. Shepard, and J. Hone, *Nat. Nanotechnol.* **5**, 722 (2010).
- ¹¹ T.T. Tran, K. Bray, M.J. Ford, M. Toth, and I. Aharonovich, *Nat. Nanotechnol.* **11**, 37 (2016).
- ¹² A.K. Geim and I.V. Grigorieva, *Nature* **499**, 419 (2013).
- ¹³ T.P. Kaloni, Y.C. Cheng, and U. Schwingenschlögl, *J. Mater. Chem.* **22**, 919 (2012).
- ¹⁴ G. Cassabois, P. Valvin, and B. Gil, *Nat. Photonics* **10**, 262 (2016).
- ¹⁵ F.H. Stephens, V. Pons, and R.T. Baker, *Dalton T.* **25**, 2613 (2007).
- ¹⁶ A.C. Stowe, W.J. Shaw, J.C. Linehan, B. Schmid, and T. Autrey, *Phys. Chem. Chem. Phys.* **9**, 1831 (2007).
- ¹⁷ S.K. Jang, J. Youn, Y.J. Song, and S. Lee, *Sci. Rep-UK* **6**, 1 (2016).
- ¹⁸ J. Liu, R.G. Kutty, and Z. Liu, *Molecules* **21**, 1636 (2016).
- ¹⁹ Z. Liu, Y. Gong, W. Zhou, L. Ma, J. Yu, J.C. Idrobo, J. Jung, A.H. MacDonald, R. Vajtai, and J. Lou, *Nat. Commun.* **4**, 1 (2013).

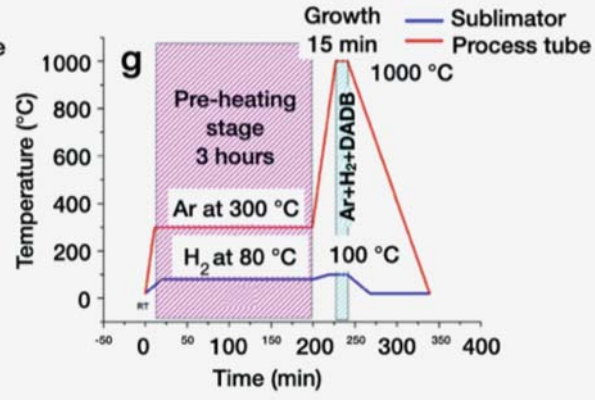
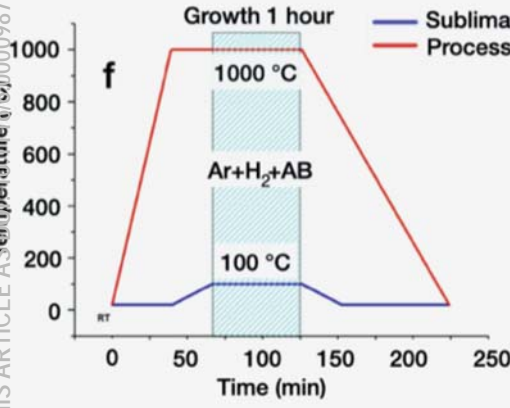
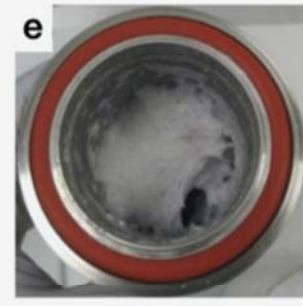
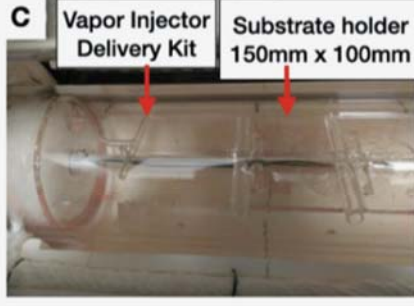
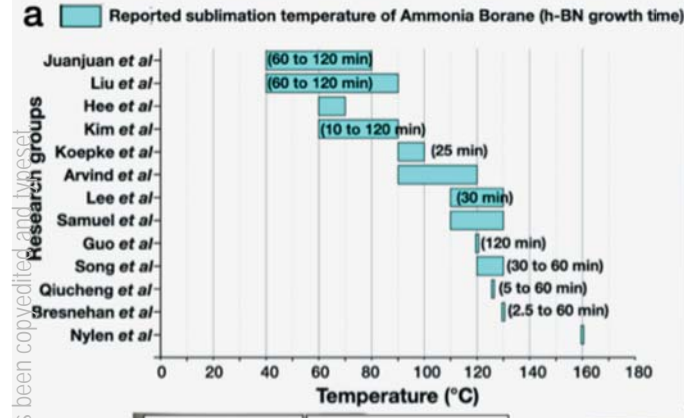
This is the author's peer reviewed, accepted manuscript. However, the online version of record will be different from this version once it has been copyedited and typeset.
PLEASE CITE THIS ARTICLE AS DOI: 10.1116/1.50000987

- ²⁰ G.H. Han, J.A. Rodríguez-Manzo, C.W. Lee, N.J. Kybert, M.B. Lerner, Z.J. Qi, E.N. Dattoli, A.M. Rappe, M. Drndic, and A.T.C. Johnson, *ACS Nano* **7**, 10129 (2013).
- ²¹ H.T. Hwang, A. Al-Kukhun, and A. Varma, *Int. J. Hydrogen Energ.* **37**, 2407 (2012).
- ²² S. Frueh, R. Kellett, C. Mallery, T. Molter, W.S. Willis, C. King'ondeu, and S.L. Suib, *Inorg. Chem.* **50**, 783 (2011).
- ²³ N. Guo, J. Wei, L. Fan, Y. Jia, D. Liang, H. Zhu, K. Wang, and D. Wu, *Nanotechnology* **23**, 415605 (2012).
- ²⁴ Q. Li, X. Zou, M. Liu, J. Sun, Y. Gao, Y. Qi, X. Zhou, B.I. Yakobson, Y. Zhang, and Z. Liu, *Nano Lett.* **15**, 5804 (2015).
- ²⁵ M.S. Bresnehan, M.J. Hollander, M. Wetherington, M. LaBella, K.A Trumbull, R. Cavalero, D.W. Snyder, and J.A. Robinson, *ACS Nano* **6**, 5234 (2012).
- ²⁶ J. Nylén, T. Sato, E. Soignard, J.L. Yarger, E. Stoyanov, and U. Häussermann, *J. Chem. Phys.* **131**, 104506 (2009).
- ²⁷ L. Britnell, R. V Gorbachev, R. Jalil, B.D. Belle, F. Schedin, M.I. Katsnelson, L. Eaves, S. V Morozov, A.S. Mayorov, N.M.R. Peres, A.H.C. Neto, J. Leist, A.K. Geim, L.A. Ponomarenko, and K.S. Novoselov, *Nano Lett.* **12**, 1707 (2012).
- ²⁸ G.H. Lee, Y.J. Yu, C. Lee, C. Dean, K.L. Shepard, P. Kim, and J. Hone, *Appl. Phys. Lett.* **99**, 243114 (2011).
- ²⁹ R. V Gorbachev, I. Riaz, R.R. Nair, R. Jalil, L. Britnell, B.D. Belle, E.W. Hill, K.S. Novoselov, K. Watanabe, T. Taniguchi, and A.K. Geim, *Small* **7**, 465 (2011).
- ³⁰ Q. Cai, D. Scullion, A. Falin, K. Watanabe, T. Taniguchi, Y. Chen, E.J. Santos, and L.H. Li, *Nanoscale* **9**, 3059 (2017).

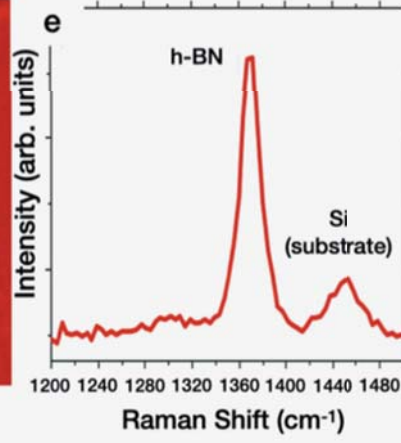
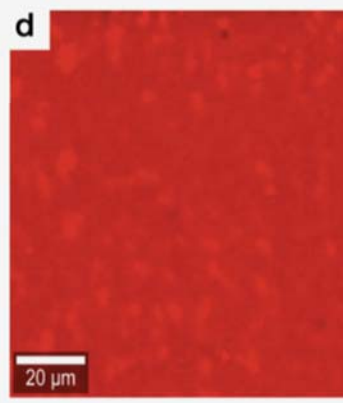
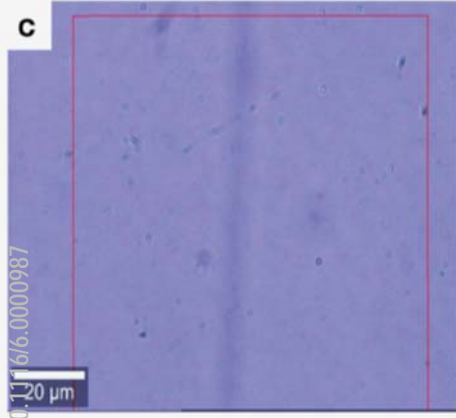
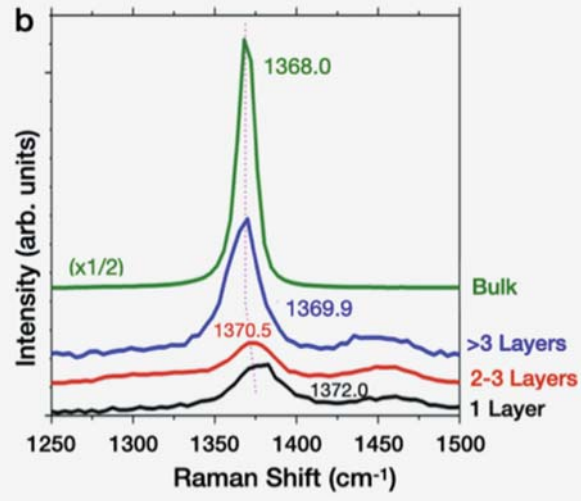
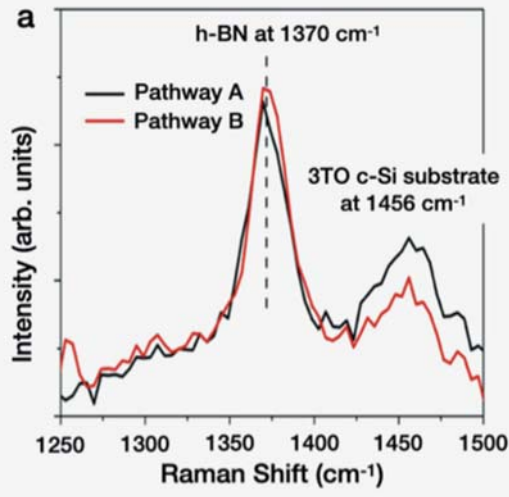
This is the author's peer reviewed, accepted manuscript. However, the online version of record will be different from this version once it has been copyedited and typeset.
PLEASE CITE THIS ARTICLE AS DOI: 10.1116/6.0000987

- ³¹ M.H. Khan, Z. Huang, F. Xiao, G. Casillas, Z. Chen, P.J. Molino, and H.K. Liu, *Sci. Rep-UK* **5**, 1 (2015).
- ³² K.P. Sharma, S. Sharma, A.K. Sharma, B.P. Jaisi, G. Kalita, and M. Tanemura, *CrystEngComm* **20**, 550 (2018).
- ³³ J. Wang, F. Ma, and M. Sun, *RSC Adv.* **7**, 16801 (2017).
- ³⁴ M. Wang, M. Kim, D. Odkhuu, N. Park, J. Lee, W.J. Jang, S.J. Kahng, R.S. Ruoff, Y.J. Song, and S. Lee, *ACS Nano* **8**, 5478 (2014).
- ³⁵ Q. Wu, S.K. Jang, S. Park, S.J. Jung, H. Suh, Y.H. Lee, S. Lee, and Y.J. Song, *Nanoscale* **7**, 7574 (2015).
- ³⁶ E. Mayer, *Inorg. Chem.* **11**, 866 (1972).
- ³⁷ M.G. Hu, J.M. Van Paasschen, and R.A. Geanangel, *J. Inorg. Nucl. Chem.* **39**, 2147 (1977).
- ³⁸ R.M. Adams, J. Beres, A. Dodds, and A.J. Morabito, *Inorg. Chem.* **10**, 2072 (1971).
- ³⁹ P.A. Storozhenko, R.A. Svitsyn, V.A. Ketsko, A.K. Buryak, and A.V. Ul'yanov, *Zh. Neorg. Khim+* **50**, 1066 (2005).
- ⁴⁰ K.H. Lee, H.J. Shin, J. Lee, I.Y. Lee, G.H. Kim, J.Y. Choi, and S.W. Kim, *Nano Lett.* **12**, 714 (2012).

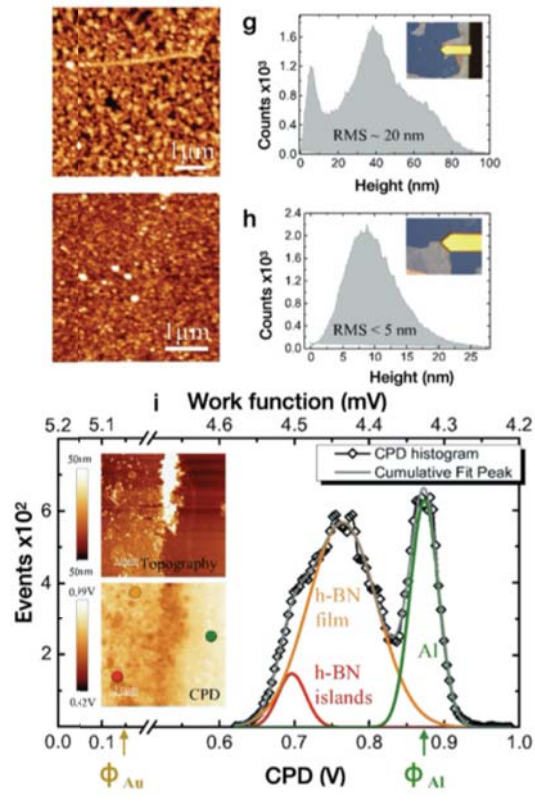
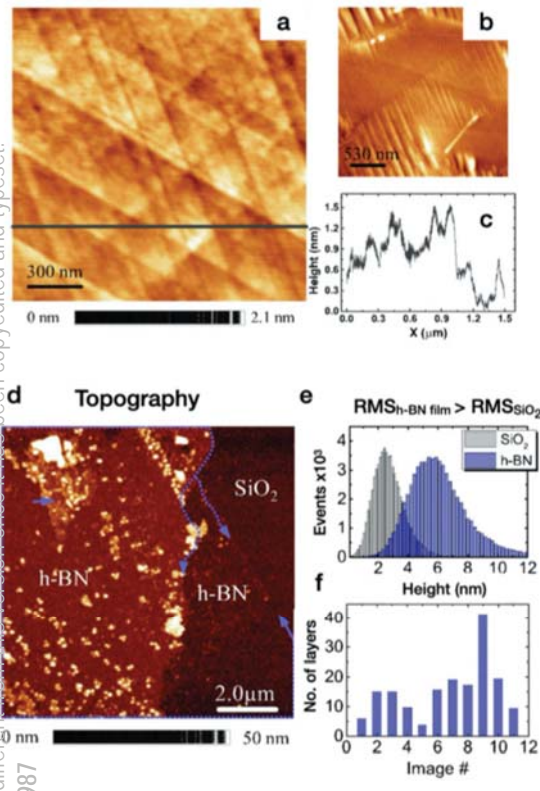
This is the author's peer reviewed, accepted manuscript. However, the online version of record will be different from this version once it has been copyedited and typeset. PLEASE CITE THIS ARTICLE AS [Temperature \(°C\)0000987](#)



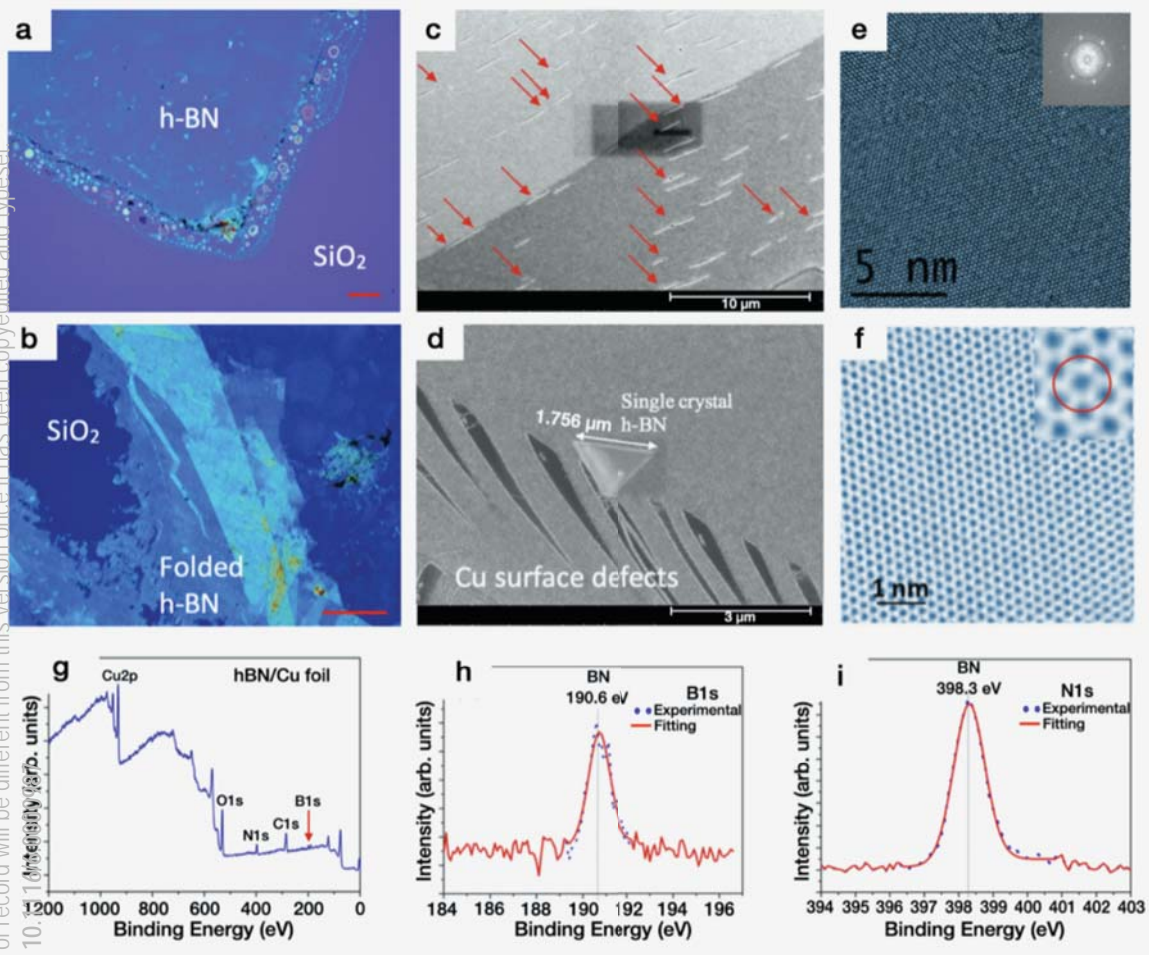
This is the author's peer reviewed, accepted manuscript. However, the online version of record will be different from this version once it has been copyedited and typeset.
PLEASE CITE THIS ARTICLE AS DOI: 10.1116/1.50000987



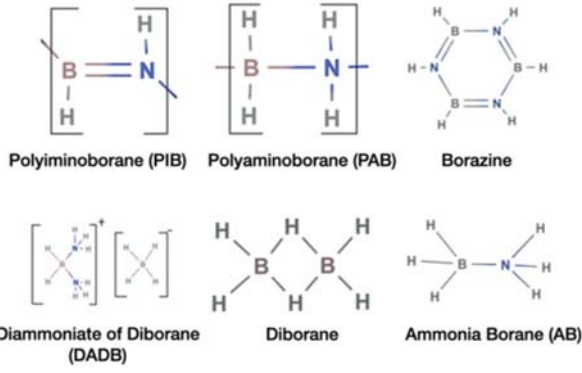
This is the author's peer reviewed, accepted manuscript. However, the online version of record will be different from this version once it has been copyedited and typeset.
PLEASE CITE THIS ARTICLE AS DOI: 10.1116/6.0000987



This is the author's peer reviewed, accepted manuscript. However, the online version of record will be different from this version once it has been copyedited and typeset.
PLEASE CITE THIS ARTICLE AS DOI: 10.1116/1.5011111



This is the author's peer reviewed, accepted manuscript. However, the online version of record will be different from this version once it has been copyedited and typeset.
PLEASE CITE THIS ARTICLE AS DOI: 10.1116/6.0000987



This is the author's peer reviewed, accepted manuscript. However, the online version of record will be different from this version once it has been copyedited and typeset.
PLEASE CITE THIS ARTICLE AS DOI: 10.1116/6.0000987

